Effect of roof heights on dynamic characteristics of wind pressure on square low-rise buildings

Authors:

Tingting Liu, MSc. CE
Northeast Forestry University, Harbin, China
Faculty of Civil Engineering
liutingting@nefu.edu.cn

Dongzhi Wang, MSc. CE
Design and research institute of the second construction limited company of China construction eighth engineering division, Jinan, China
wdzfxr@163.com

Hongfu Zhang, PhD. CE
Northeast Forestry University, Harbin, China
Faculty of Civil Engineering
zhanghongfu@nefu.edu.cn
Corresponding author

Prof. **Dabo Xin**, PhD. CE
Northeast Forestry University, Harbin, China
Faculty of Civil Engineering
xindabo@nefu.edu.cn

Original scientific paper

<u>Tingting Liu, Dongzhi Wang, Hongfu Zhang, Dabo Xin</u>

Effect of roof heights on dynamic characteristics of wind pressure on square low-rise buildings

The high suction induced by strong wind on a flat roof can result in severe local damage or even in the overturning of the entire roof. The roof height has a significant effect on characteristics of the high wind suction force. The wind pressure on flat roofs of various heights is investigated in this paper. The extreme wind pressure and its position are firstly studied at different wind incidence angles. Proper orthogonal decomposition (POD) and coherence function analyses are then conducted to analyse dynamic characteristics. The results show that the local extreme pressure increases with an increase in roof height. The fluctuation of the separation bubble also increases, and there exists a mode competition of the first two POD modes. On the contrary, the roof height has fewer effects on conical vortices. In addition, two coherent regions (conical vortices) are observed on the roof. Although these two regions have small correlation coefficients, they have a considerably high coherence function at low frequency. These results are expected to contribute to better understanding of high suction characteristics on flat roofs, and can potentially provide guidance for avoiding roof damage induced by strong wind suction.

Key words:
wind pressure, flat roof, conical vortices, various roof heights

Izvorni znanstveni rad

<u>Tingting Liu, Dongzhi Wang, Hongfu Zhang, Dabo Xin</u>

Utjecaj visine krova na dinamička svojstva djelovanja vjetra kod niskih zgrada kvadratnog tlocrta

Veliko usisavanje inducirano jakim vjetrom na ravnom krovu može izazvati ozbiljna lokalna oštećenja ili čak prevrtanje čitavog krova. Krovna visina značajno utječe na svojstva velike sile usisavanja vjetra. U ovom radu ispitan je utjecaj tlaka vjetra na ravne krovove različitih visina. Ekstremne vrijednosti pristiska vjetra i njegov položaj prvi su proučavani i to pri različitim kutovima djelovanja vjetra. Provedene su pravilna ortogonalna dekompozicija (POD) te analize funkcije koherentnosti kako bi se analizirala dinamička svojstva. Rezultati pokazuju da se povećanjem krovnih visina povećava i lokalni ekstremni tlak. Povećava se i oscilacija područja odvajanja te postoji i nadmetanje između prvih dvaju modova POD-a. Nasuprot tome, krovne visine imaju manji utjecaj na ljevkaste vrtloge. Štoviše, na krovu su proučavana i dva usklađena područja (ljevkasta vrtloga). Iako ta dva područja imaju male vrijednosti korelacijskih koeficijenata, imaju veliku koheziju pri niskim frekvencijama. Dobiveni rezultati mogu pomoći pri boljem razumijevanju utjecaja velikog usisavanja na ravne krovove te potencijalno omogućiti izbjegavanje šteta na krovovima koje nastaju snažnim usisavanjem vjetra.

Ključne riječi:
pritisak vjetra, ravan krov, ljevkasti vrtlozi, različite krovne visine

1. Introduction

With an increasing demand for low and long-span buildings (terminals, industrial workshops, etc.), flat roof low-rise buildings with smaller aspect ratios are nowadays being constructed quite extensively. Low-rise buildings, immersed in the bottom of the atmospheric boundary layer, have complex flow and aerodynamic characteristics. Owing to the sharp edge, flow separation always occurs near the leading edge of the roof and leads to an adverse pressure gradient downstream of the roof edge [1, 2]. The shear layer flow separation that results from the adverse pressure gradient is accompanied by formation of a variety of vortices, the most well-known being the separation bubble and conical vortices [3, 4]. When wind direction is perpendicular to the leading edge, the separation bubble, which leads to high suction, is always generated near the leading-edge. When wind direction is oblique to the leading edge, conical vortices form [5] and give rise to increased wind loads. These two coherence structures on the roof, resulting in peak suction (extreme negative pressure), can cause severe damage to structures and can even result in overturning of the entire roof when the roofing system lacks sufficient strength [6, 7]. Moreover, the complex vortex structures acting on the low-rise building always cause non-uniform distribution of the wind pressure on the roof. In other words, wind loads are closely related to the vortices on the roof. Therefore, it is necessary to study the wind loads and flow field characteristics of low-rise-building roofs.

Because the local wind pressure is closely associated with the separation bubbles and conical vortices on the roof, numerous researchers have investigated these two coherence structures [8-10]. The separation bubble is generated as the incoming flow separates from the leading edge of the building, and strong suction is generated near the leading edge of flat roof. Kim quantified characteristic dimensions of the separation bubble in various cross sections of a three-dimensional prism using the particle image velocimetry (PIV) technique [8]. He pointed out that the turbulent kinetic energy maximum occurs in the separation layer at the upper boundary of the separation bubble near the leading edge of the top plate, and that the magnitude of the maximum energy is approximately 2.5 times that of the trailing region. Pratt and Kopp investigated the separation bubble and the induced wind pressure of a low-rise building through synchronized pressure and velocity measurements [9]. They reported that peak pressures for varying surface areas and locations on the roof are associated with reattachment lengths, or separation bubbles, of varying sizes. Near the leading edge, the reattachment length scales (separation bubble size) of these regions relate to the size of the area average and the location of the area. For a small area near the leading edge, the reattachment occurs at approximately 20 % of the mean reattachment length. Peak suctions are associated with the locally accelerated flow near the leading edge of the building, which scales with the size and location of the roof surface area over which the pressures are integrated. Akon and Kopp investigated the effects of turbulence intensity and boundary layer thickness on the mean reattachment length of a low-rise building by PIV [10]. It was discovered that the mean size of the roof separation bubble was not influenced by the turbulence length scale, while the turbulence intensity had a significant effect on the reattachment length. The conical vortex is created because the airflow released from the vertical side rolls up [11]. The location of the conical vortex and its characteristics have been studied in recent years. Lin et al. conducted wind tunnel pressure measurements on flat-roof models of varying sizes. They found that the suction force along the wind direction angle decayed exponentially under the action of a conical vortex [12]. Based on the analysis of the mean and fluctuating wind pressure of a low-rise building, Kawai and Nishimura investigated the vortex core and reattachment position of the conical vortex on a flat roof under the action of uniform and turbulent flow fields [13]. They concluded that the two most obvious forms of motion of the conical vortex axis are the low-frequency swaying motion and the high-frequency rotational motion. The angle between the conical vortex axis and the windward leading edge in the smooth flow is greater than that in the turbulent flow. Marwood and Wood conducted synchronized pressure measurements on a cubic model and found that the conical vortex constantly changed in the horizontal and vertical directions [14]. Chun et al. investigated conical vortex on the flat roof of a low-rise building to obtain the vortex volume field, velocity field, and turbulent kinetic energy of the vortex at various wind angles by using PIV [15]. The results show that a wind angle of 30° is the most unfavourable wind direction, and that the vortex volume and turbulent kinetic energy of the unilateral conical vortex reach the maximum value for all cases. Sun and Ye investigated the conical vortices generated at the corner regions of large-span flat roofs by using PIV [16]. The location of the leading edge corresponding to the negative peak vorticity and maximum turbulent kinetic energy was found at the centre of the conical vortex. The wind pressure reaches the maximum near the leading-edge roof corner, and a triangle of the severe suction zone appears downstream. Kozmar studied the surface pressure on a cubic building underlying conical vortices [5]. He found that a larger mean suction could be observed on the top cube surface in the less turbulent boundary layer. With an increase in turbulence, the strong suction zones decreased in size and the fluctuating pressure coefficient was observed to be larger in more turbulent flows.

The shape of a low-rise building has a considerable influence on the vortices and the wind loads induced on its roof [17, 18]. The roof height is one of the most important factors affecting the flow field around a low-rise building. Many studies have shown that it has a significant effect on the vortex structures of buildings. For high-rise and mid-rise buildings, the effects of height on the flow field and the crosswind and along-wind forces on the building are more important. By using the smoke visualization techniques, two types of vortices were found

for the formation and shedding of wall-mounted cylinders [19]. Kármán-type vortex shedding predominates at the height to width ratios greater than 2; otherwise, arch-shaped vortex shedding is more likely. Wang et al. investigated Karman-type and arch vortex shedding typical flow topologies of two prism models in greater depth with height–width ratios of 2 and 6 using the PIV technique [20]. Elsharawy et al. performed wind pressure tests with varying wind directions on four building models (full size heights: 6, 12, 25, and 50 m) and at varying heights in an open exposed terrain to estimate the instantaneous base shear and torsional moments, which were used to obtain the mean and peak values of shear and torsional coefficients for different heights [21]. Sumner et al. investigated the effects of the height to width ratio on the flow field by numerical simulation [22]. It was found that the critical height to width ratio of the prism is 3, and that the flow field around the prism is significantly different below the critical height to width ratio of the prism.

However, the effect of the roof height on the flow field and its surface pressure has not been systematically studied for flat-roof low-rise buildings. Again, flat-roof low-rise buildings with smaller aspect ratios, such as industrial plants, are constructed quite frequently; hence, it is necessary and meaningful to conduct a detailed study on the dynamic wind pressure characteristics prevailing on these roofs. Doing so can provide guidance to avoid roof damage induced by strong wind suction. The wind surface pressure on flat roofs of varying height is systematically investigated in this study. The extreme pressure, mean pressure, and fluctuating pressure, are studied in the first part of the paper. The POD and coherence function analyses are then conducted to study dynamic characteristics of flat-roofs of varying heights.

2. Experimental setup and data acquisition

Wind tunnel tests for pressure measurements on low-rise buildings were conducted for this database in the boundary layer wind tunnel at Tokyo Polytechnic University, Japan (more details can be found at [23]. The wind tunnel is 2.2 m wide and 1.8 m high. The length scale was set at 1/100. As the velocity scale was assumed at 1/3, the time scale can be estimated at 3/100. The height of 10 cm from the floor is set as a reference height. The Japanese suburban terrain is simulated in the boundary layer wind tunnel, which corresponds to the type III terrain according to Architectural Institute of Japan - AIJ, 2004. The mean wind speed profile index for this category is 0.2 (see Figure 2), the gradient height is 450 m. In Figure 2, U (z) and I (z) respectively denote the wind speed and turbulence intensity at height Z. The mean wind speed and the turbulence
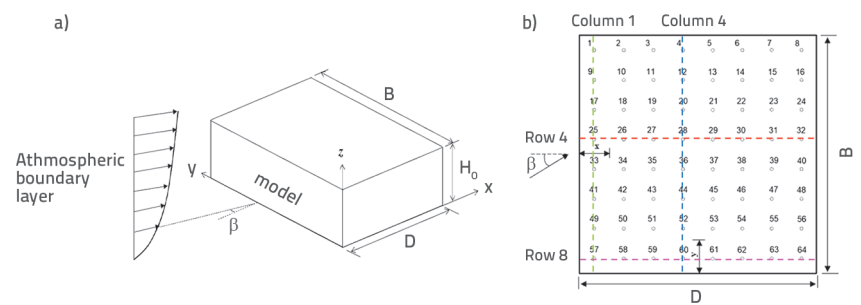

Figure 1. a) Geometrical parameters and coordinate system of the model; b) position of measured taps of the flat roof

intensity profiles were measured at the centre of the turntable in the wind tunnel. It was simulated with turbulence-generating spires, roughness elements and a carpet on the upstream floor of the wind tunnel's test section. The turbulence intensity at the reference height is 25 %. The test wind velocity at the reference height is about 7.4 m/s, corresponding to about 22 m/s at a height of 10m in full scale. The uniformity of flow along the cross section of the tunnel and the homogeneity in the flow direction was checked before pressure measurement tests.

The pressure measurement model of the low-rise building is shown in Figure 1.a. H_0, B, and D represent the height, width, and depth of the building, respectively. The width of the model is 160 mm, the aspect ratio is B : D = 1 : 1, and the height–width ratios are H_0/B = 1 : 4, 2 : 4, 3 : 4, and 4 : 4. Seven different wind incident directions were measured for each configuration: $\beta = 0°$, 15°, 30°, 45°, 60°, 75°, and 90°. Wind pressure measurement taps were evenly arranged on the roof of the tested model. The positions of the measured taps and their numbers are shown in Figure 1.b. Synthetic resin tubes 80cm long and 1.2 mm in internal diameter connected each tap with a pressure measurement Scanivalve, which can measure the fluctuating wind pressures at 384 points nearly synchronously. The sampling frequency was 500 Hz and the sampling period was 18 seconds for each sample, corresponding to 15Hz and 10 minutes in full scale. Each test case was sampled 10 times. The pressure data from the wind tunnel test of the flat roof model were analysed in this study.
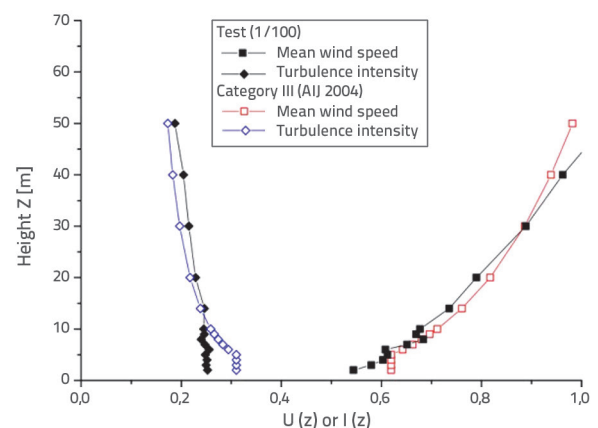

Figure 2 Simulated wind fields of the suburban terrain [27]

3. Results and discussion

3.1. Wind pressure characteristics of roofs

In the pressure measurement experiment, the time history of the wind pressure coefficients is calculated as

$$Cp(i,t) = p(i,t) / p_H \qquad (1)$$

where $Cp(i,t)$ is the wind pressure coefficient at measured tap i and at time t, $p(i,t)$ is the pressure measured at pressure tap i and at time t, and p_H is the reference dynamic pressure at the roof height, H, where $p_H = 0.5\rho V_H \cdot V_H$. The mean and fluctuating pressure coefficients are defined as follows:

$$\overline{C_p} = \frac{1}{N}\sum_{i=1}^{N} C_p(t_i) \qquad (2)$$

$$C_p' = \frac{1}{N}\sqrt{\sum_{i=1}^{N}(C_p(t_i) - \overline{C_p})^2} \qquad (3)$$

The extreme local pressure coefficient as a function of the incidence angle β and the corresponding location label are shown in Figure 3, where $-c_{pmin}$ and c'_{pmax} denote the minimum pressure coefficient (extreme local pressure coefficient) and the maximum fluctuating pressure coefficient of the model roof, respectively. The minimum pressure, $-c_{pmin}$, considers the probability distribution function and is modified appropriately according to the "Cook–Mayne coefficient" [24]. Based on the extreme pressure coefficient of the extreme distribution type I, the minimum pressure coefficient is modified as follows:

$$C_{pmin} = \overline{C_p} \times c_{ad} \qquad (4)$$

$$c_{ad} = 1 + 0{,}636\, V_x \qquad (5)$$

where c_{ad} is the adjustment factor, V_x is the variable coefficient, $V_x = s/m$. σ is the rms-value of the extremes, and m is the mean value of the extremes. $\overline{C_p}$ is the mean pressure coefficient.

Figure 3.a shows that the maximum wind suction of the roof is more sensitive to the roof height and wind incidence angle. In contrast, the position of the extreme pressure coefficient is unchanged with various roof height and wind incidence angles, which always occur at the corner (tap 57) or the position slightly deviating from the corner (tap 49 or 58). There are two peaks of the extreme pressure coefficient with various wind incidence directions, and the maximum peak occurs at β = 30° except H_0/B = 3 : 4, whose position slightly deviates from the corner (tap 49), which has similar results with Kim et al and Tieleman [15, 25]. Furthermore, the maximum peak value increases as the roof height ratio increases, and the maximum peak value reaches 3.6 at H_0/B = 4 : 4. This is more than two times the mean value. This indicates that under the inclined wind angle, extremely stronger wind suction is applied in roof corner with larger roof height. With respect to the fluctuating wind pressure coefficients shown in Figure 3(b), there is only one peak value for various β(located at β = 45°), which is different from the results in Figure 3.a. However, the results of the cases at β= 30° resemble those shown in Figure 3.a. The fluctuating pressure increases with an increase in roof height.

Figure 4 shows the wind pressure distribution on the model roof at 0° and 30° wind directions. Generally, the mean pressure pattern shares similar features to the fluctuating pressure both in the case of β = 0° and β = 30°. As shown in Figure 4.a1, for a wind incidence angle of 0°, the incoming flow past the buildings produces the separation bubble, with large negative pressure and strong fluctuations, occurs at the leading edge of the roof. The closer to the leading edge, the higher and more drastic the pressure gradient. Furthermore, the corner has the maximum mean and fluctuating wind pressure. As the roof height ratio increases, the mean and fluctuating pressure also increase,
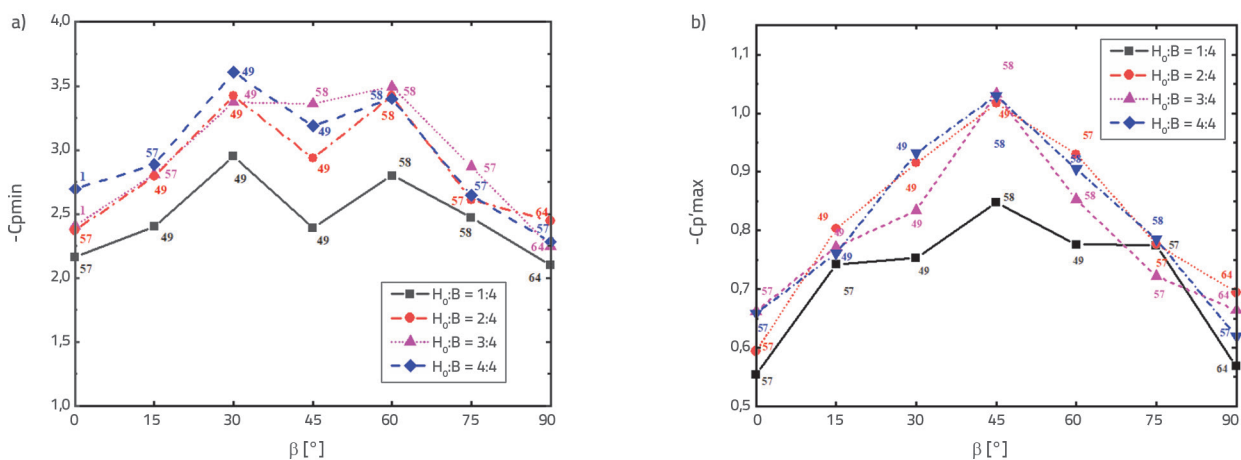

Figure 3. a) The minimum pressure coefficient ($-c_{pmin}$) varies with the wind incidence angle (β); b) maximum fluctuating pressure coefficient (c'_{pmax}) varies with the wind incidence angle (β). Note: measured on the flat roof with different values of the height-width ratio H_0/B
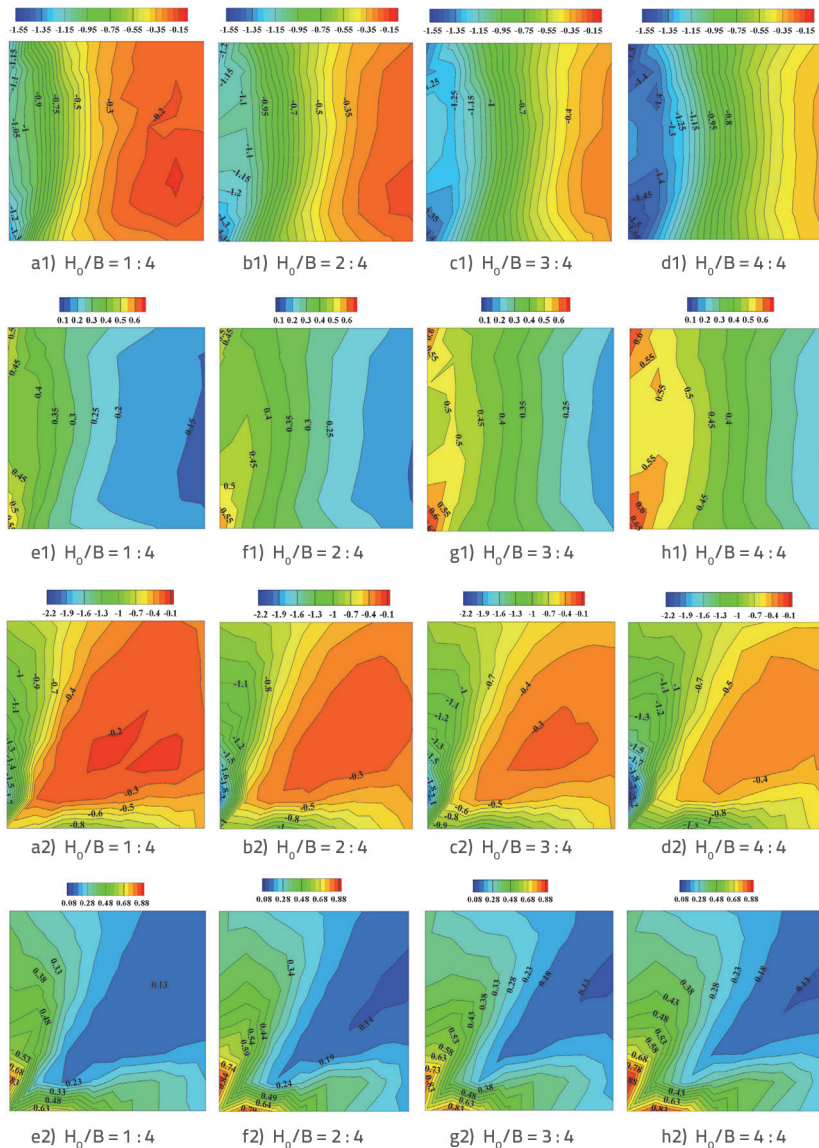
Figure 4. Mean pressure coefficients on the roof for $H_0/B = 1:4 \sim 4:4$ at 0° wind direction angle it is shown as (a1) - (d1), and fluctuating pressure coefficients as (e1) - (h1); at 30° wind direction angle it is shown as (a2) - (d2), and fluctuating pressure coefficients as (e2) - (h2). Labels on the graphs denote the pressure coefficient values

To quantify further the wind pressure on the roof, the downwind pressure in Row 4 (shown in Figure 1.b) on the roof was selected for analysis. The mean and fluctuating pressure curves are plotted in Figure 5. For the case of β = 0°, the high negative mean pressure on the roof is the separation bubble. Clearly, the separation bubble covers almost the entire roof. Furthermore, the measurement tap is from the windward leading edge, and the wind suction and fluctuating pressure show a decreasing trend, as in Figures 5(a) and 5(b). Moreover, the wind suction increases significantly with an increase in the roof height near the leading edge (X/D < 0.4), while the fluctuating pressure increases over the entire range. For β = 30°, as the measurement tap moves farther from the windward leading edge, the wind suction and the fluctuating pressure sharply decrease and then gradually increase, as in Figures 5.c and 5.d. Moreover, the wind suction and the fluctuating pressure slightly increase as the roof height increases. This indicates that the effect of the roof height on the separation bubbles is greater than that on the conical vortices. In other words, separation bubbles on a roof are more sensitive to the low-rise building roof height than conical vortices.

Here, the downwind pressure in Column 4 (shown in Figure 1.b) on the roof was selected for analysis. The mean and fluctuating pressure curves were plotted, as shown in Figure 6. For β = 0°, the separation bubble almost covers the entire leading edge. Owing to the interference of the side edge on the bubble, the wind suction and fluctuating pressure of the inner part are slightly higher than those close to the side edge, as shown in Figures 6.a and 6.b, indicating that the bubble is weakened near the side edges. Moreover, the wind suction and fluctuating pressure increase significantly with an increase in the height to width ratio. However, for β = 30°, the wind suction and the fluctuating pressure change little with an increase in roof height. This confirms that the separation bubbles on a roof are more sensitive to the low-rise building height than conical vortices. The total lift force is more sensitive to the low-rise building height at β = 0° than at β = 30°.

especially at the corner, which can be attributed to the effects of side edge. Different with the case at β = 0°, the corner of the roof appears to have higher suction on one side than on the other, and two asymmetrical conical vortices appear as shown in Figure 4.a2, with higher suction in the vortex region. As the roof height increases, the mean pressure also increases, and the pattern is becoming increasingly asymmetric about the diagonal line, while the fluctuating pressure does not follow the same rule. Moreover, the maximum mean and fluctuating wind pressure occurs at a position slightly deviating from the corner, which can explain the phenomenon shown in Figure 3.a.
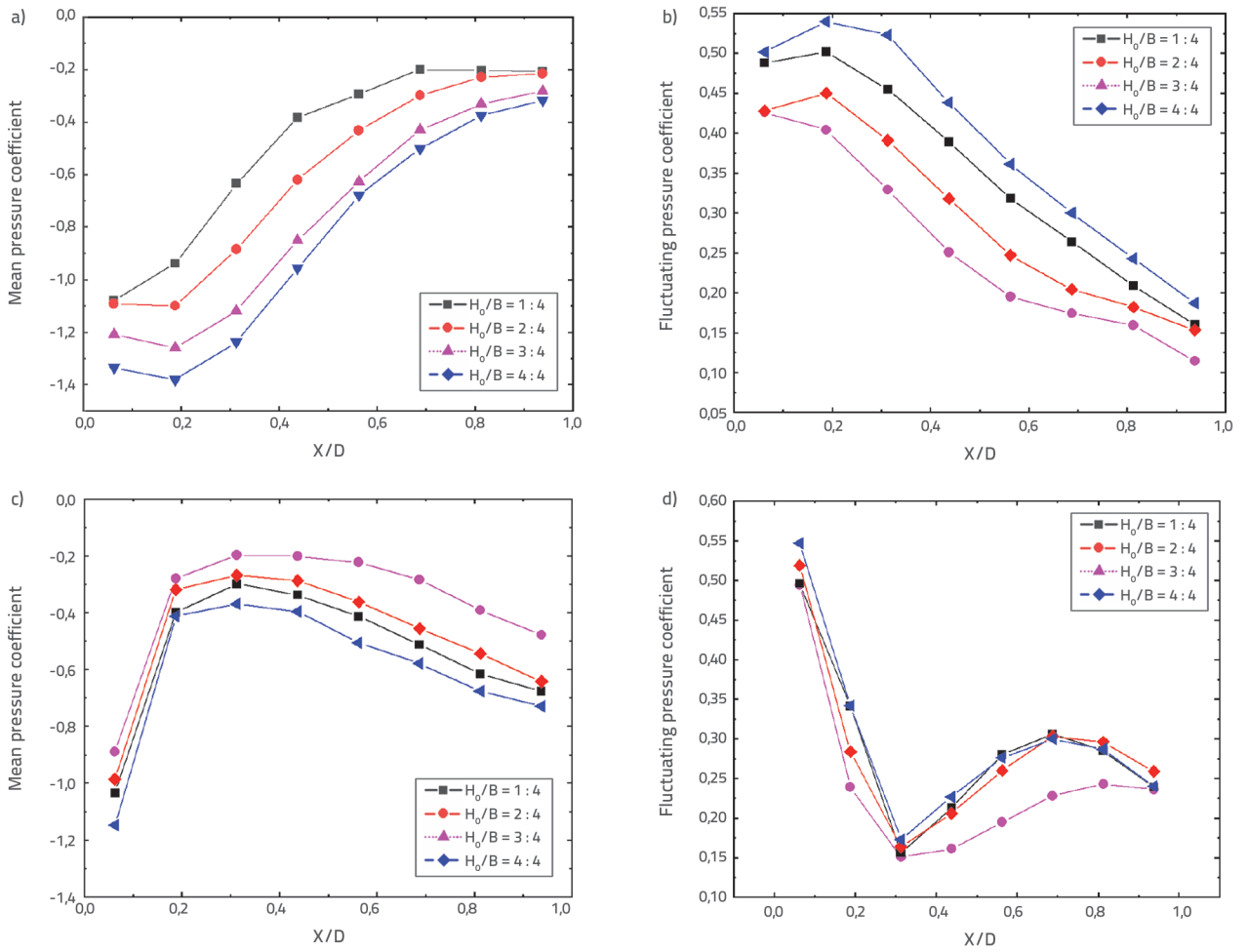
Figure 5. Mean and fluctuating pressure coefficient distributions at various H_0/B: a) 0° wind angle; b) 0° wind angle; c) 30° wind angle; d) 30° wind angle
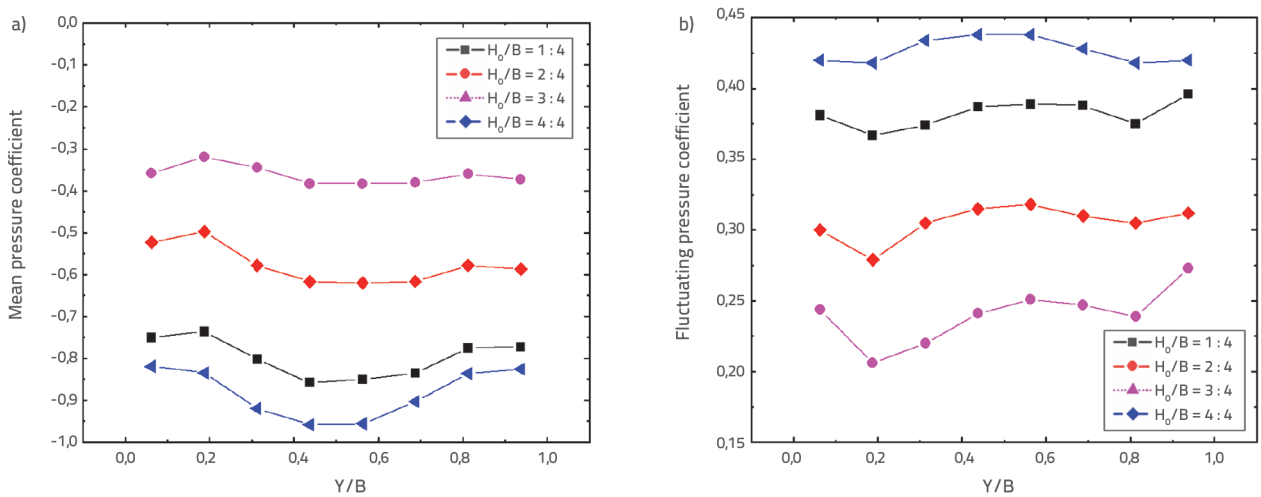

Figure 6. Mean and fluctuating pressure coefficient distribution for various H_0/B: a) 0° wind angle; b) 0° wind angle (the first part of the Figure 6)
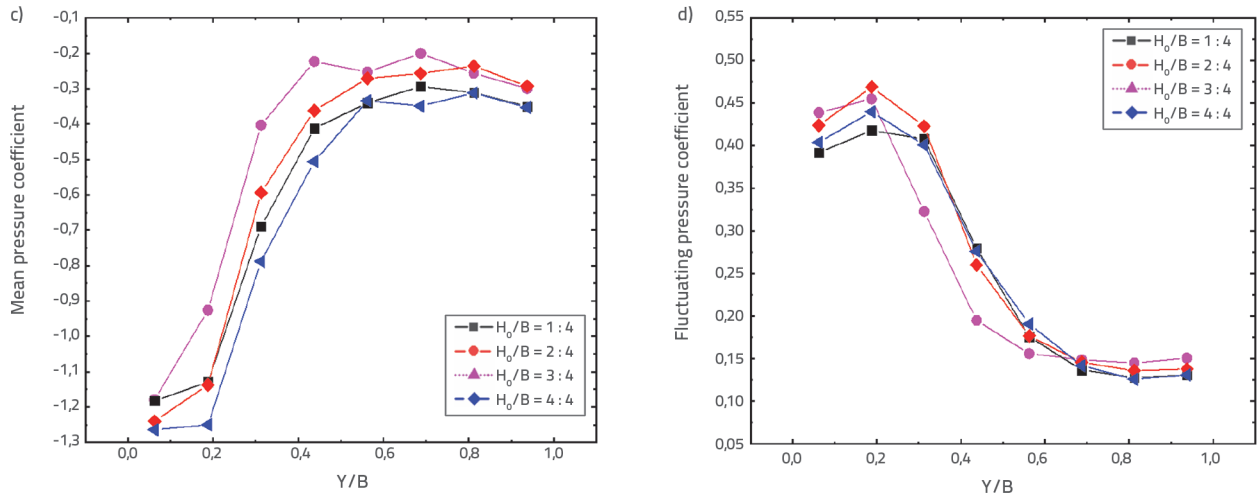
Figure 6. Mean and fluctuating pressure coefficient distribution for various H_0/B: c) 30° wind angle; d) 30° wind angle (continuation of the Figure 6)

3.2. Wind pressure power spectrum

The fluctuating wind power spectra of extreme negative pressure tap 1 and tap 49 at 0° and 30° wind directions are shown in Figures 7(a) and 7(b), respectively, under different roof heights. Here, $f \cdot H/U$ is the dimensionless frequency, and $f \cdot S(f)/\sigma^2$ represents the value of the dimensionless self-power spectrum. f is the frequency, H is the roof height, and U is the wind speed at the roof height. $S(f)$ is the measurement tap wind pressure self-spectrum, and σ^2 is the variance of the fluctuating wind pressure. Horizontal coordinates are expressed in logarithmic coordinates so that the curve decay and distribution of energy can clearly be observed. At a wind incidence angle of 0°, the fluctuating wind pressure power spectrum at the position of tap 1 has obvious broad-spectrum characteristics. The peak value is clearly observed at $f \cdot H/U \approx 0.3$ for $H_0/B = 1 : 4$, which represents a predominance of small-scale turbulent components. With an increase in roof height, the spectral peak moves from the mid-frequency to the low-frequency, especially for $H_0/B = 4 : 4$ with $f \cdot H/U \approx 0.12$. This implies that the turbulent

component of the small-scale part gradually decreases, and that the turbulent component of the large-scale part gradually increases. The small-scale turbulence component is generated by the unsteady reattachment and rolled during formation of the separation bubble, indicating that the size of the separation bubble is enhanced with an increase in roof height, and the scale increases gradually. The positions of spectral peaks have no obvious regulation for the 30° wind incidence angle, and they all occur in the middle- and high-frequency range. Most of the incoming wind energy is converted into the high-frequency rotational motion of the conical vortex.

3.3. POD analysis of fluctuating pressure fields

The POD is a space–time separated analysis method that decomposes the structural wind pressure field into time-dependent principal coordinates and space-dependent eigenmodes. The POD technique was applied to the fluctuating pressure field of the roofs to study in more depth the wind field characteristics of roofs of varying roof heights. Here, the POD
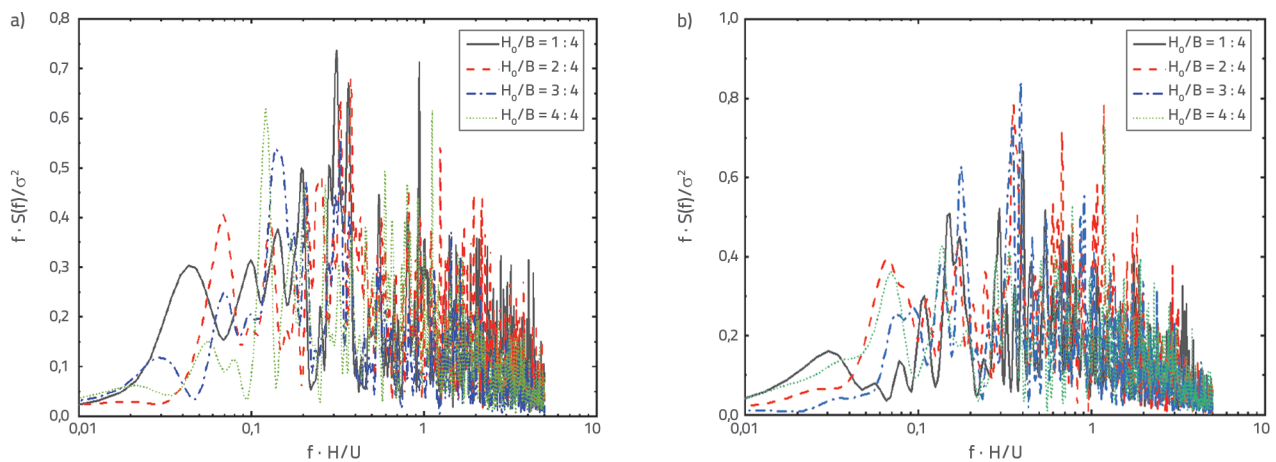

Figure 7. Power spectrum of: a) tap 1, 0° wind angle; b) tap 49, 30° wind angle
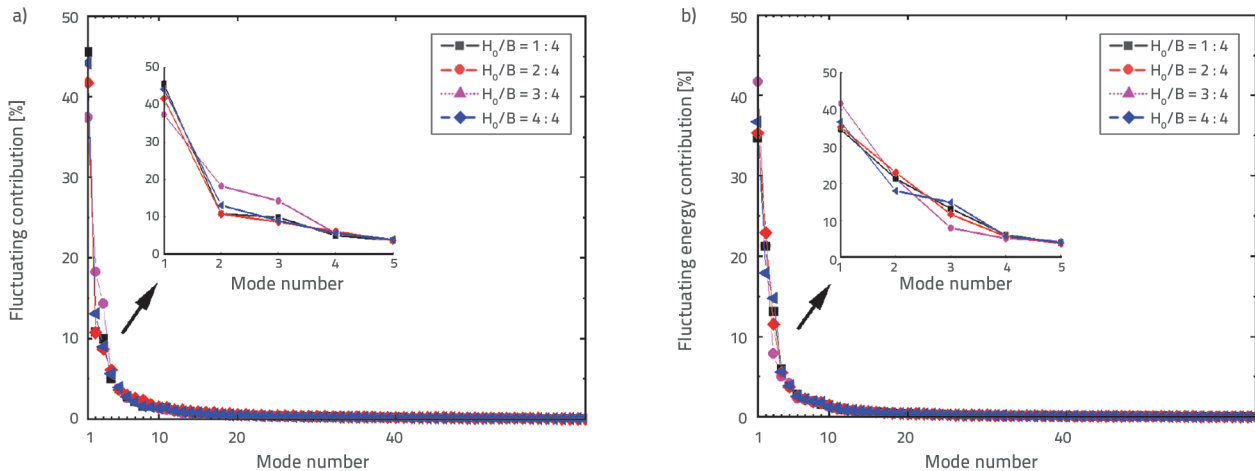
Figure 8. Fractional contribution to fluctuating energy from different POD modes : a) 0° wind angle; b) 30° wind angle

analysis is briefly introduced. The pressure measurement taps are uniformly distributed on the roof, and the spatial covariance of the pressure is expressed as Equation (4), which is the wind pressure covariance at various measurement tap locations.

$$R_p(x,y,x',y') = \overline{p(x,y,t)p(x',y',t)} \qquad (6)$$

The maximum value of the projection of $p(x, y, t)$ on the function of $\phi(x, y)$ is expressed in the mean square sense, and it yields an eigenvalue problem [26].

$$R_p f = lf \qquad (7)$$

where the eigenvalues λ_n and eigenvectors $\phi_n(x, y)$ can be obtained by solving this equation. After using the eigenvector orthogonalization process, the pressure field can be expressed as:

$$p(x,y,t) = \sum_{m=1}^{M} a_m(t)\phi_m(x,y) \qquad (8)$$

where $a_m(t)$ is the principal coordinate. Because these functions are optimal in the mean square sense and the modes are ranked according to their eigenvalue, the POD requires only a small number of terms in the expansion to describe the random field more accurately.

The fractional contribution to the fluctuating energy from different POD modes at (a) $\beta = 0°$ and (b) $\beta = 30°$ is shown in Figure 8. For $\beta = 0°$, the first mode accounts for approximately 40 % of the total fluctuating energy, and the fractional contribution decreases rapidly with an increase in the number of POD modes. The contribution of the first mode to the total fluctuating energy increases with an increase in roof height, while the contribution of the higher modes doesn't follow the same rule or even the inverse rule. It means the lower the roof the pressure tends to be more chaotic, as the mode energy becomes more dispersive, which may result from the ground effect. At $\beta = 30°$, the first modes with different roof heights, as shown in Figure 8(b), have similar fractional contribution as at $\beta = 0°$, while the difference is that $H_o/B = 1 : 4$ has the highest fractional contribution. At $\beta = 30°$, the slope rate from the first mode to the second mode is much higher than that at $\beta = 0°$, which indicates that the conical vortex generated at oblique wind direction is more complex than the vortex structures generated at normal wind direction. As stated above, the eigenvalues represent contribution of the corresponding POD modes to the total turbulence fluctuation energy. The first five eigenvalues of the modes and the sum of all eigenvalues are given in Tables 1 and 2, corresponding to $\beta = 0°$ and 30°, respectively. For $\beta = 0°$, the eigenvalues of the first five modes increase with an increase in roof height, especially for the eigenvalues of the first mode, which is of principal

Table1. First five eigenvalues of pressure fluctuation for four aspect ratios at $\beta = 0°$

Eigenvalues				
Mode	1 : 4	2 : 4	3 : 4	4 : 4
1	2.377	2.812	4.194	4.870
2	0.473	0.666	1.070	1.444
3	0.407	0.553	0.855	0.989
4	0.315	0.404	0.471	0.620
5	0.176	0.277	0.328	0.420
Sum of all eigenvalues	3.748	4.662	6.918	8.343

Table2. First five eigenvalues of pressure fluctuation for four aspect ratios at β = 30°

Eigenvalues				
Mode	1 : 4	2 : 4	3 : 4	4 : 4
1	2.795	2.907	2.665	3.108
2	1.425	1.886	1.63	1.517
3	0.525	0.95	1.005	1.250
4	0.332	0.453	0.457	0.475
5	0.278	0.304	0.291	0.331
Sum of all eigenvalues	5.355	6.500	6.048	6.681

significance for representing the fluctuating pressure fields [27]. Apparently, the mode energy at $H_0/B = 4 : 4$ is more than twice as high as that at $H_0/B = 1 : 4$. This means that the wind pressure fluctuation of the roof becomes more drastic with an increase in roof height. For β = 30°, the second mode eigenvalues for different roof heights are generally larger than β = 0° in Table 2 and they exhibit great fluctuating energy. This implies that the contribution of the high order modes to the total fluctuating energy can not be negligible, and that conical vortices make the pressure fields more chaotic.

The contours of the first three modes for the four cases at β = 0° and β = 30° are shown in Figure 9 and Figure 10, respectively. It should be noted that the pressure mode in different positions fluctuates in phase for a certain POD mode, and that they are only the function of physical coordinates. Their time-depended oscillating magnitude is only determined by the principal coordinate defined in Eq. 8. In other words, the POD mode represents the relative fluctuating values among the points. For the first mode at β = 0°, the pressure fluctuation values at the windward leading edge of the roof are large at $H_0/B = 1 : 4$, and the fluctuation gradually concentrates in the windward corner region of the roof as the roof height. This coincides with the location of the extreme pressure coefficient obtained by measurement in the previous section. With respect to the second mode, positive and negative pressure fluctuations occur symmetrically at the windward corners for $H_0/B = 1 : 4$. For $H_0/B = 2 : 4$, the fluctuating pressure is weakened in one of the corners, while the other is strengthened. As the roof height increases, the corner of the larger fluctuating pressure expands to the full leading edge of the roof, which resembles the first mode of the case of $H_0/B = 4 : 4$. In other words, the first two modes exchange places as the roof height increases.

With respect to β = 30°, the first three modes show that the fluctuation appears only at the windward side of the leading edge, which is close to the corner, and, with an increase in roof height, the larger fluctuating pressure expands to another windward side, as shown in the case of $H_0/B = 2 : 4$. In general, the peak value of all modes always occurs near the corner, which indicates that the roof corner area has the strongest fluctuations.
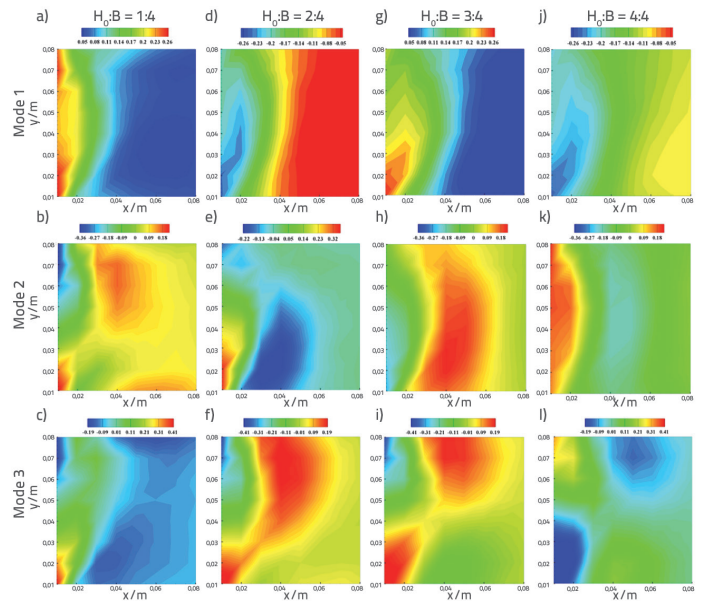

Figure 9. Contours of POD modes 1–3 for $H_0/B = 1 : 4, 2 : 4, 3 : 4$, and $4 : 4$ at 0° wind direction: $H_0/B = 1 : 4$ (a–c), $H_0/B = 2 : 4$ (d–f), $H_0/B = 3 : 4$ (g–i), and $H_0/B = 4 : 4$ (j–l)
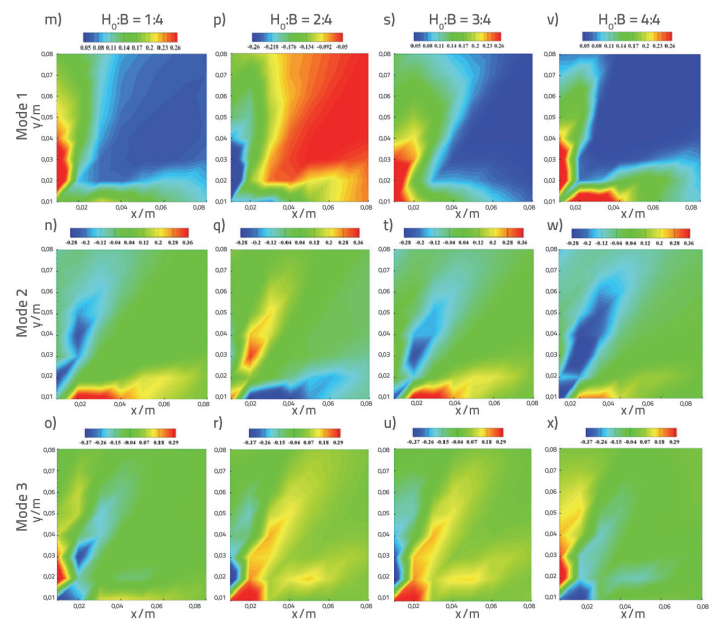

Figure 10. Contours of POD modes 1–3 for $H_0/B = 1 : 4, 2 : 4, 3 : 4$, and $4 : 4$ at 30° wind direction: $H_0/B = 1 : 4$ (m–o), $H_0/B = 2 : 4$ (p–r), $H_0/B = 3 : 4$ (s–u), and $H_0/B = 4 : 4$ (v–x)

In addition, the overall shapes of the first three modes are not sensitive to roof height.

3.4. Correlation analysis

The spatial correlation coefficient between measurement taps at different locations is a measure of the spatial correlation between two referent points in the time domain. It is useful to understand the spatial correlation of wind pressure between the extreme pressure point and each measurement point. The spatial correlation coefficient is defined as

$$Cor_{ij} = \frac{\sigma_{ij}}{\sigma_i \sigma_j} \tag{9}$$

where σ_{ij} is the wind pressure covariance at taps i, j, and σ_i and σ_j are the variance of wind pressure at referent points I and j, respectively.
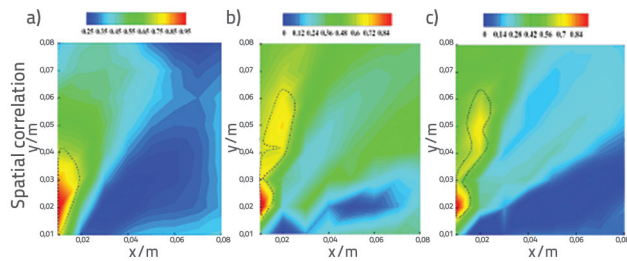

Figure 11. Spatial correlation coefficients on the roof at: a) 0° b) 30°; c) 45°: the reference is tap 49

The spatial correlation analysis of the full area of the roof was carried out for the extreme pressure referent point (tap) 49 under different wind incidence angles for the height-width ratio of 1 : 4, as shown in Figure 11. The red region represents the strongly correlated region, and the spatial correlation in this region is significant, while the blue region indicates the weak correlation region. It is clear that the weak correlation region is located at the other side of the diagonal line of the roof. Compared with the other cases, the case of β = 30° has the largest influence area. The wind-sensitive locations are at the corner of the roof and at the leading edge of the windward side. To explore the vortex characteristics at the wind-sensitive locations more closely, the fluctuation coherence of Column 1 at 0° and at 30° and Row 8 at 30° is given in the frequency domain as follows. The coherence function r^2_{ij} can be defined as

$$r^2_{ij} = \frac{\left|S_{ij}(f)\right|^2}{S_i(f)S_j(f)} \tag{10}$$

where $S_{ij}(f)$ is the cross-power spectrum between referent points i and j; $S_i(f)$ and $S_j(f)$ stand for the auto power spectrum of referent points i and j, respectively.

The thick solid lines in Figures 12.b, 12.d and 12.f represent the locations of extreme pressure referent points (RP) 1, 49, and

58, respectively. The coherence function contour is in a striped distribution overall, and, the closer it is to the referent point, the stronger the coherence.
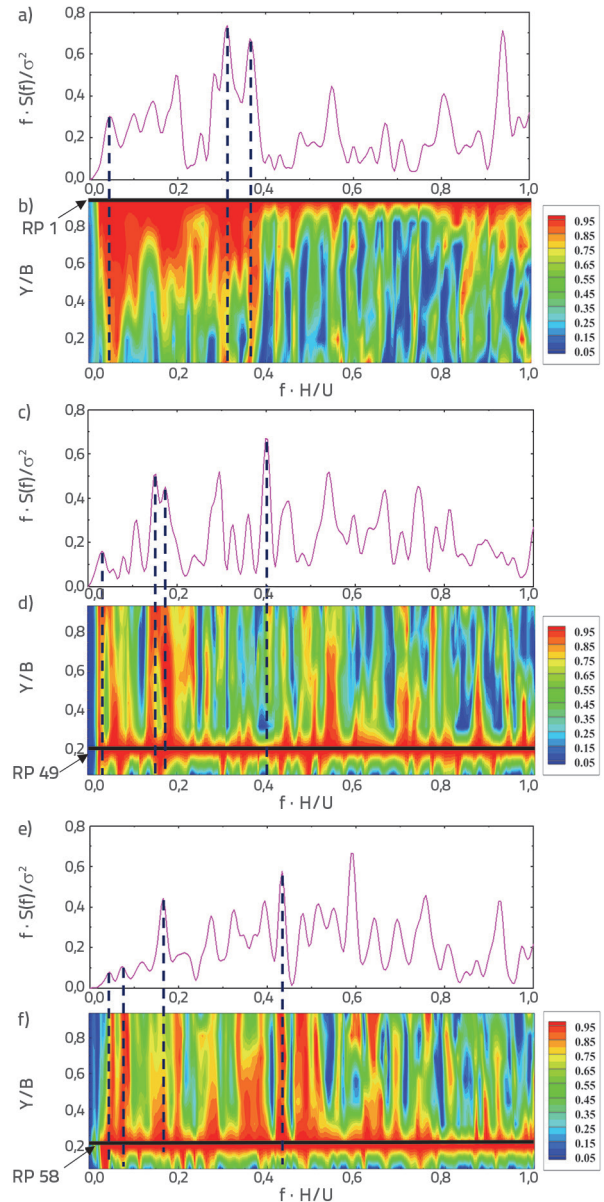

Figure 12. Power spectral density (lines) and coherence function contours for referent point 1, $H_0/B = 1 : 4$, Column 1 ($H_0/B = 1 : 4$, β = 0°) (a, b); referent point 49, Column 4 ($H_0/B = 1 : 4$, β = 30°) (c, d); and referent point 58, Row 8 ($H_0/B = 1 : 4$, β = 30°) (e, f)

Figure 12.b shows that there is a broadband characteristic in the dimensionless frequency range of 0–0.5, and that the low-frequency vortex runs through the whole leading edge, corresponding one by one to the power spectrum peaks of measurement referent point 1. Most of the energy spectrum peaks are concentrated in the low-frequency range, indicating that the first column of the measurement points is inside the
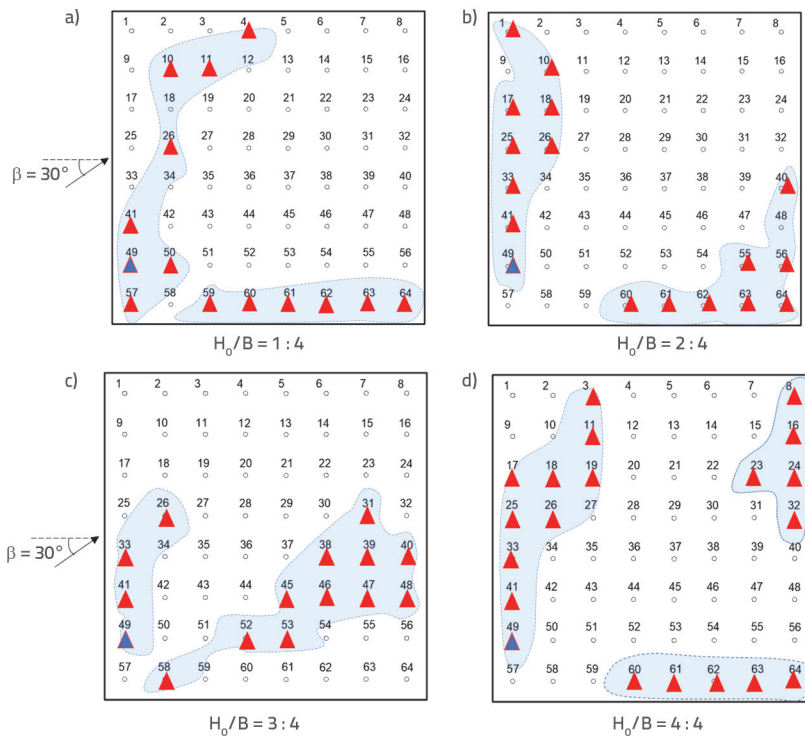
Figure 13. Coherence of each measurement point for referent point 49 at a 30° wind angle: a) $H_0/B = 1 : 4$; b) $H_0/B = 2 : 4$; c) $H_0/B = 3 : 4$; d) $H_0/B = 4 : 4$

Clearly, these regions are generated by large-scale conical vortices. Although these regions have a small correlation coefficient, as shown in Figure 13, they have a high low-frequency coherence function. This indicates that the spatial coherence function is not always the decreasing function of distance, implying that the synchronicity of wind loads in the two regions should be considered at the design stage.

4. Conclusion

The wind pressure on flat roofs was systematically investigated at different roof heights for low-rise buildings. The extreme wind pressure and its positions were first studied for four roofs at different wind incidence angles. The POD and coherence function analysis were used to analyse dynamic characteristics (spatial shape and frequency) and conical vortices. The following conclusions can be drawn:

same large-scale separation bubble; the turbulence inside the separation bubble is intense, and there is a strong coherence between the measurement points at the windward leading edge. In Figure 12.d, the energy spectrum is approximately evenly distributed in all frequency bands, and there is penetration even in the low-frequency band. Although the high frequency of $f·H/U = 0.4$ corresponds to the largest peak of the power spectral density, it is not in the same vortex as referent point 49. This indicates that the left conical vortex consists of dominated large-scale coherent vortices (low frequency) and some small-scale incoherent vortices (high frequency) at 30°. In Figure 12.f, spectral peaks occur at low and high frequencies, and many penetrate throughout Row 8. This implies that large high-frequency vortices account for a major part of the right conical vortex.

Here, the coherence of the roof measurement taps with different roof heights at a 30° wind angle and the extreme referent point 49 is explored. The coherence between the referent points on the roof and the extreme referent point 49 marked with a blue triangle for different roof heights at a 30° wind angle for each measurement tap is shown in Figure 13. The focus here is on the taps with a coherent frequency interval of 0.05–0.1 (focus on large-scale vortices) and a coherence function greater than 95 %, with the taps marked with red triangles. The range of coherent regions is plotted, and pressure fluctuations at the measurement taps within the range are maintained at a high-level coherence function. Two coherent regions are distributed at all four roof heights on both sides of the diagonal.

- The magnitude of the roof extreme wind suction is closely related to the roof height of the building and wind incidence angle. However, the positions of the extreme pressure coefficient are unchanged at various heights and wind incidence angles, which always occur at the corner or the position slightly deviating from the corner. There are two peaks of the extreme pressure coefficient with various wind incidence directions. The maximum peak occurs at β = 30° with the position slightly deviating from the corner. Furthermore, the maximum peak value increases with an increase in height.
- Separation bubbles on low-rise building roofs are highly influenced by the height of low-rise buildings compared to conical vortices. The separation bubbles strengthen and the range increases with an increase in roof height, and the fluctuation energy of the large-scale turbulence increases accordingly.
- At a wind incidence angle of 0°, the eigenvalues of the first mode increase the most with an increase in roof height, and the pressure fluctuations at the leading edge of the roof become increasingly intense. The first two modes exchange positions as the roof height increases, which means that the mode completion exists. At a wind incidence angle of 30°, the roof height has a limited effect on the mode shape and energy.
- There are two coherent regions at all four roof heights, ant they are distributed on both sides of the diagonal. These two regions are generated by large-scale conical

vortices. Although these two regions have a small correlation coefficient, they have a high low-frequency coherence function, which indicates that the spatial coherence function is not always the decreasing function of distance, implying that the synchronicity of wind loads in the two regions should be considered at the design stage. In addition, the roof height has a limited effect on the coherent regions.

Acknowledgements

REFERENCES

[1] Richards, P.J., Hoxey, R.P., Short, L.J.: Wind pressures on a 6m cube, Journal of Wind Engineering & Industrial Aerodynamics, 89 (2001) 14, pp. 1553-1564.

[2] Pindado, S., Meseguer, J.: Wind tunnel study on the influence of different parapets on the roof pressure distribution of low-rise buildings, Journal of Wind Engineering & Industrial Aerodynamics, 91 (2003) 9, pp. 133-1139.

[3] Tieleman, H.W.: Wind tunnel simulation of wind loading on low-rise structures: a review, Journal of Wind Engineering & Industrial Aerodynamics, 91 (2003) 12, pp. 1627-1649.

[4] Su, N., Sun, Y., Wu, Y., Shen S.Z.: Three-parameter auto-spectral model of wind pressure for wind-induced response analysis on large-span roofs, Journal of Wind Engineering & Industrial Aerodynamics, 158 (2016), pp. 139-153.

[5] Kozmar, H.: Surface pressure on a cubic building exerted by conical vortices, Journal of Fluids & Structures, 2020, 92.

[6] Mertol, H.C., Tunc, G., Akis, T.: Evaluation of masonry buildings and mosques after Sivrice earthquake, GRAĐEVINAR, 73 (2021) 9, pp. 881-892, https://doi.org/10.14256/JCE.3101.2021

[7] Čokić, M., Folić, R.: Fragility and robustness analysis of a multistorey RC building, GRAĐEVINAR, 73 (2021) 1, pp. 27-44, https://doi.org/10.14256/JCE.3036.2020

[8] Kim, K.C., Ji, H.S., Seong, S.H.: Flow structure around a 3-D rectangular prism in a turbulent boundary layer, Journal of Wind Engineering & Industrial Aerodynamics, 91 (2003) 5, pp. 653-669.

[9] Pratt, R.N., Kopp, G.A.: Velocity field measurements above the roof of a low-rise building during peak suctions, Journal of Wind Engineering & Industrial Aerodynamics, 133 (2014), pp. 234-241.

[10] Akon, A.F., Kopp, G.A.: Mean pressure distributions and reattachment lengths for roof-separation bubbles on low-rise buildings, Journal of Wind Engineering & Industrial Aerodynamics, 155 (2016), pp. 115-125.

[11] Banks, D., Meroney, R.N., Sarkar, P.P., Zhao, Z., Wu, F.: Flow visualization of conical vortices on flat roofs with simultaneous surface pressure measurement, Journal of Wind Engineering & Industrial Aerodynamics, 84 (200) 1, pp. 65-85.

[12] Lin, J.X., Surry, D., Tieleman, H.W.: The distribution of pressure near roof corners of flat roof low buildings, Journal of Wind Engineering & Industrial Aerodynamics, 56 (1995) 2, pp. 235-265.

[13] Kawai, H., Nishimura, G.: Characteristics of fluctuating suction and conical vortices on a flat roof in oblique flow, Journal of Wind Engineering & Industrial Aerodynamics, 60 (1996), pp. 211-225.

[14] Marwood, R., Wood, C.J.: Conical vortex movement and its effect on roof pressures, Journal of Wind Engineering & Industrial Aerodynamics, 69 (1997), pp. 589-595.

[15] Kim, K.C., Ji, H.S., Seong, S.H.: PIV measurement of roof corner vortices, Wind and Structures, 4 (2001) 5, pp. 441-454.

[16] Sun, H.J., Ye, J.H.: 3-D characteristics of conical vortex around large-span flat roof by PIV technique, Wind and Structures, 22 (2016) 6, pp. 663-684.

[17] Aly, A.M., Khaled, F., Gol-Zaroudi, H.: Aerodynamics of Low-Rise Buildings: Challenges and Recent Advances in Experimental and Computational Methods, Aerodynamics, 2020.

[18] Liu, Z.X., Yu, Z.X., Chen, X.X., Cao, R.Z., Zhu, F.: An investigation on external airflow around low-rise building with various roof types: PIV measurements and LES simulations, Building and Environment, 2020, pp. 169.

[19] Sakamoto, H., Arie, M.: Vortex shedding from a rectangular prism and a circular cylinder placed vertically in a turbulent boundary layer, J. Fluid Mech, 126 (1983) 1, pp.147-165.

[20] Wang, F., Lam, K.M., Zu, G.B., Cheng, L.: Coherent structures and wind force generation of square-section building model, Journal of Wind Engineering & Industrial Aerodynamics, 188 (2019), pp. 175-193.

[21] Elsharawy, M., Galal, K., Stathopoulos, T.: Torsional and shear wind loads on flat-roofed buildings, Engineering Structures, 84 (2015) feb.1, pp. 313-324.

[22] Sumner, D., Rostamy, N., Bergstrom, D.J., Bugg, J.D.: Influence of aspect ratio on the mean flow field of a surface-mounted finite-height square prism, International Journal of Heat and Fluid Flow, 2017, 65 (2017) Jun., pp. 1-20.

[23] http://www.wind.arch.t-kougei.ac.jp/info_center/windpressure/lowrise/mainpage.html)

[24] Cook, N.J., Mayne, J.R.: A refined working approach to the assessment of wind loads for equivalent static design, Journal of Wind Engineering & Industrial Aerodynamics, 6 (1980) 1, pp. 125-137.

[25] Tieleman, H.W.: Pressures on surface-mounted prisms: The effects of incident turbulence, Journal of Wind Engineering & Industrial Aerodynamics, 1993.

[26] Bienkiewicz, B., Tamura, Y., Ham, H.J., Ueda, H., Hibi, K.: Proper orthogonal decomposition and reconstruction of multi-channel roof pressure, Journal of Wind Engineering & Industrial Aerodynamics, 1995.

[27] Fu, J.Y., Wu, J.R., Liang, S.G.: Wind tunnel testing of wind pressures on a large gymnasium roof, Journal of Central South University, 18 (2011) 002, pp. 521-529.

[28] TPU Aerodynamic Database, http://www.wind.arch.t-kougei.ac.jp/info_center/windpressure.html, 2013.